Ceramics International xxx (xxxx) xxx

Contents lists available at ScienceDirect

Ceramics International

journal homepage: www.elsevier.com/locate/ceramint

Effect of microstructure on the thermal conductivity of thermal barrier coating deposited by chelate-flame spraying

YanXin Dan [a,b,c], Yu Wang [c], Atsushi Nakamura [c], Hidetoshi Saitoh [c], Hua Li [a,b,*]

[a] Key Laboratory of Marine Materials and Related Technologies, Zhejiang Key Laboratory of Marine Materials and Protective Technologies, Ningbo Institute of Materials Technology and Engineering, Chinese Academy of Sciences, Ningbo, 315201, China

[b] Zhejiang Engineering Research Center for Biomedical Materials, Cixi Institute of BioMedical Engineering, Ningbo Institute of Materials Technology and Engineering, Chinese Academy of Sciences, Cixi, 315300, China

[c] Department of Materials Science and Technology, Graduate School of Engineering, Nagaoka University of Technology, 1603-1 Kamitomioka-machi, Nagaoka, Niigata, 940-2188, Japan

ARTICLE INFO

Keywords:
Thermal barrier coating
Microstructure
Thermal conductivity
Chelate-thermal spray
Thermal insulation capability

ABSTRACT

To reveal the structure-property relationships of the microstructure and the thermal conductivities of the coatings, Er_2O_3 coatings were directly deposited on an aluminum alloy substrate without bond coating by chelate flame spraying (CFS). The thermal insulation capability, thermal conductivity, microstructure, porosity, and splats of each coating were studied as a function of thickness. The coating with a thickness of 300 μm exhibited a high ΔT value that was 43.1% higher than that of the 100 μm-thick coating deposited with the same spray conditions. The 100 μm-thick coating exhibited low thermal conductivity, which decreased from 4.56 $Wm^{-1}K^{-1}$ to 2.57 $Wm^{-1}K^{-1}$ in the semistable phase (500 °C and 600 °C); this was mainly due to its special microstructure, which contained more mesh splats and higher porosity (28.3%) than the 300 μm-thick coating. Moreover, the effects of the microstructure on the thermal insulation capacities of the CFS coatings were determined. The results showed that as-deposited thick coatings offered higher heat conduction in the studied temperature range (from room temperature to 600 °C) than thin coatings. To conclude, this study also provides a new test method to determine thermal conductivity and thermal insulation capacity.

1. Introduction

Thermal barrier coatings (TBCs) are widely used to protect heated sections of aero- and land-based gas turbines from thermal, corrosion, and erosion effects and significantly enhance the durability of components or increase working temperatures to achieve better engine performance and efficiency [1–6]. Typical TBCs are double-layer coatings applied to protect components, and they consist of a metallic bond coating and a ceramic topcoat [7,8]. The main function of the bond coat is to protect the substrates from oxidation and corrosion during thermal treatment [9]. Ceramic coatings have relatively low thermal conductivities that can reduce the need for cooling systems [10]. Generally, ceramic surface coatings are deposited with plasma spraying techniques [11,12]. Traditional plasma-sprayed ceramic coatings exhibit a lamellar structure with large, connected gaps and high porosity, which is why they enhance insulation performance and lower the thermal conductivity [13]. However, high energy consumption and large-scale installation requirements limit the further application of these methods [14]. Therefore, the development of a new flame-spraying system for synthesizing TBCs providing good thermal insulation and high-temperature stability is still of both scientific significance and technological importance.

Recently, a new deposition technique using a metal-ethylenediaminetetraacetic acid (EDTA) complex was reported [15,16]. In this technique, metal-EDTA complex powders are introduced using a flame-spraying method, so we call this method chelate flame spraying (CFS). These complex powders decomposed and oxidized in the flame and formed metal oxide particles, which were subsequently deposited on the substrate. In this method, metal oxide coatings with thicknesses of 9.7–13.5 μm and cross-sectional porosities of 1.6–33% were deposited on stainless steel and aluminum alloy substrates [17,18]. The metal oxide films deposited on the metal substrate were formed

* Corresponding author. Key Laboratory of Marine Materials and Related Technologies, Zhejiang Key Laboratory of Marine Materials and Protective Technologies, Ningbo Institute of Materials Technology and Engineering, Chinese Academy of Sciences, Ningbo, 315201, China.
E-mail addresses: dan_yanxin@nimte.ac.cn (Y. Dan), lihua@nimte.ac.cn (H. Li).

https://doi.org/10.1016/j.ceramint.2022.01.173
Received 15 November 2021; Received in revised form 7 January 2022; Accepted 16 January 2022
Available online 20 January 2022
0272-8842/© 2022 Elsevier Ltd and Techna Group S.r.l. All rights reserved.

from EDTA complexes added through a H_2–O_2 flame. Furthermore, the carrier gas type, powder feed ratio, and substrate temperature play important roles in determining the microstructure, including the shapes and sizes of pores and gap sizes between splats of the sprayed coatings. Based on the abovementioned, the thermal conductivity of a porous ceramic coating depends on the intrinsic thermal conductivity of the material, which is based on its composition and structure, as well as on the architecture of the porous network leading to enhanced thermal insulation. In addition, it has been reported that deposited metal-oxide coatings exhibit strong adhesion and good thermal shock performance on aluminum alloys and stainless steel substrates [15,19]. A series of studies was based on comparisons between coatings produced with different spray conditions, such as substrate temperature, carrier gas type and powder feed ratio; this allowed us to demonstrate that there was a relationship between pore sizes and shapes and natural porosity and thermophysical properties, but there is still a need to establish quantitative correlations with microstructure thermal conductivity to achieve optimal design [20].

In the present study, TBC coatings with different porosities and thicknesses were synthesized on an aluminum alloy substrate by appropriately manipulating the variables controlling CFS processes. The microstructural features and thermal insulation capabilities of the deposited coatings were investigated to provide a foundation for improving TBC properties. In addition, thermal response (laser flash method) tests were conducted on TBCs with various porosities, and thermal conductivities were calculated.

2. Experimental

2.1. Chelate flame-spraying process

We first prepared EDTA·Er·H (Chubu Chelest Co., Ltd.) for deposition of Er_2O_3 thick coatings. Fig. 1 shows the experimental setup for deposition of a TBC made from the EDTA·Er·H complex. The reacted particles were then sprayed onto an aluminum alloy substrate (A5052, 50 × 50 × 10 mm^3) that had been previously blasted by #60-grit alumina (99.7% purity, 212–250 lm particle size, Fuji Manufacturing, Fujioka, Japan), resulting in the deposition of a metal oxide film with the thermal insulation capability test. Moreover, the substrate surface was cleaned with acetone twice and dried in air. A conventional flame-spray apparatus consisting of a feed unit (5 MPE, Sulzer Metco, Westbury, NY) and spray gun (6P-II, Sulzer Metco) was used for reactive spraying. This apparatus is used commercially for the deposition of TBCs with H_2–O_2 flames. A rotation apparatus capable of depositing 12 samples (dodecahedral pattern) at a time was fabricated in-house. The rotation velocity of the apparatus was kept at 90 rpm. As stated above, we employed different carrier gases and standoff distances with the substrate to determine the effects on the microstructures of coatings. Five different types of samples were sprayed in this work, as shown in Table 1. One type of sample was sprayed with O_2 carrier gas, and it was designed to provide a coating (sample (a)) with a thickness of 100 μm and a porosity of 10%. The second (sample (b)) and third (sample (c)) samples were sprayed with N_2 carrier gas, and both sets of conditions were the same. One of the coatings was designed to exhibit improved porosity, and liquid nitrogen was used as a substrate coolant. These samples were prepared from syntheses giving porosities of 20 and 30%. Finally, two other samples (samples (d) and (e)) were sprayed with the same spray parameters as samples (b) and (c), and only the thicknesses were varied.

2.2. Characteristics

Cross-sectional morphologies and microstructures of the coatings were observed using field-emission scanning electron microscopy (FE-SEM) (JSM-6700F, JEOL). At least 6 SEM images with magnifications of 200x and 400x were randomly acquired and used for each sample. The coating thickness was the average thickness of 20 transverse sections and was estimated by analyzing the whole SEM image with the commercial software SmileView, and the porosity of the coating was evaluated based on analyses of 2D images via ImageJ software. The average thicknesses and porosities of the coatings were estimated from over 5 images randomly selected from among the polished cross-sections.

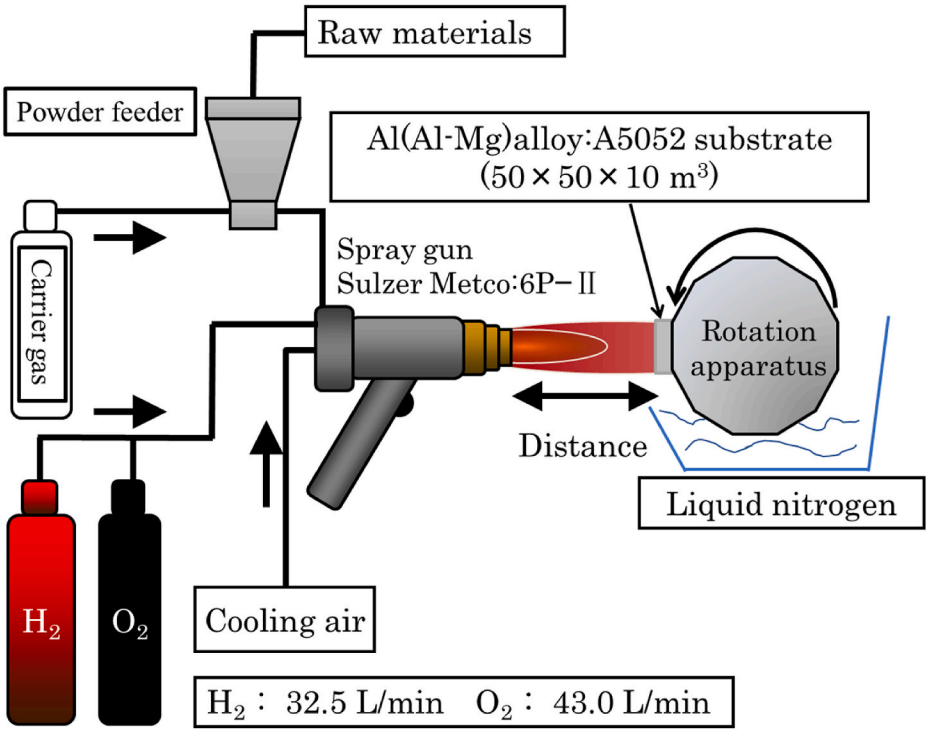

Fig. 1. Schematic of the deposition coating setup.

Table 1
Spraying parameters.

Sample	Materials	Flow rates of powder (g/min)	Carrier gas types	Flow rates of carrier gas (SCFH)	Distance (mm)	Rolling velocity (rpm)	Liquid nitrogen
(a)	EDTA・Er・	20	O_2	10	100	90	None
(b)	H	10	N_2		130		None
(c)		10	N_2		130		Yes
(d)		10	N_2		130		None
(e)		10	N_2		130		Yes

2.3. Thermal conductivity measurements

A schematic diagram of the thermal conductivity testing of coatings is shown in Fig. 2(a). The parameters of the heating source were the same as those previously described (Fig. 1) for a H_2–O_2 flame. The TBC samples or substrate samples were fixed in the rotation apparatus, and the rotational velocity was kept at 60 rpm. The surfaces of the TBC samples or the substrate samples were heated by a H_2–O_2 flame, and the back sides of the samples were placed in the rotation apparatus. Two K-type thermocouples were used as sensors: one was located on the sample surface to measure the surface temperature (coating surface temperature, $T_1 = T_{1s}$(substrate) = T_{1c}(coating)), and the other was fixed on the back side of the sample to collect these surface temperatures ($T_2 = T_{2s}$(substrate) = T_{2c}(coating)). The K-type thermocouples were linked to a wireless high-speed thermocouple temperature function logger (SHTDL4-Hispeed) to record the heating temperature curves (T_1, T_2) for 60 s in real time. For scientific purposes, the surface temperature was recorded 100 times at 1 rpm (1 s) to construct the change curve. The temperature data were analyzed and stored by a computer. In this study, the two temperature stages were analyzed as rising curves, and the stable curves and temperatures for drops across the sample and substrate (T_1-$T_2 = \Delta T_s$, ΔT_c) and across the TBCs (ΔT_s - ΔT_c) were calculated. In addition, the thermal conductivities of coatings were measured by the AC calorimetric method [21]. Fig. 2(b) shows a schematic diagram for the measurement principles of the AC calorimetric method with stages I and II. The phase difference (Φ) is calculated by the time lag (Q) and one cycle (P). In a simplified approach, when the coating thickness is greater than 10 μm, the thermal diffusivity (α) can be calculated using Eqs. (1) and (2) [22]:

$$\Phi = \sqrt{\frac{\pi f}{\alpha_s}}x \tag{1}$$

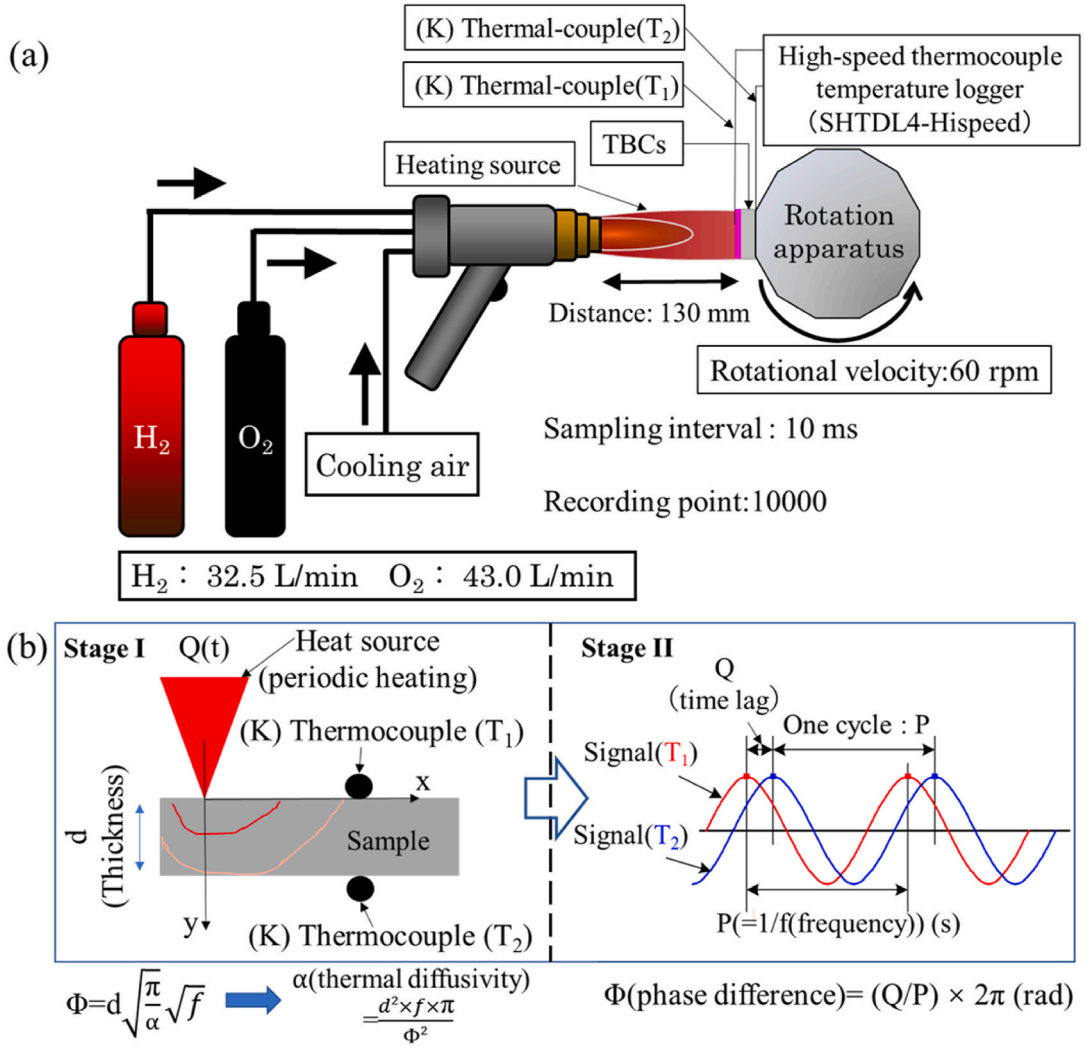

Fig. 2. Schematic diagram: (a) thermal conductivity testing of coatings and (b) phase difference (ϕ) calculation method for samples.

$$\Phi = d\sqrt{\frac{\pi}{\alpha_c}}\sqrt{f} \quad (2)$$

where θ is the phase difference in each curve (T_1 and T_2), d is the thickness of the coating, f is the frequency of the thermal cycle, α_s and x are the thermal diffusivity and thickness of the substrate, respectively, and α_s is the thermal diffusivity of the coating. Eq. (1) states that the phase difference (Φ) may be determined from the substrate thickness (x) and frequency (f), which are obtained during thermal cycling, and then, the substrate thermal diffusivity (α_s) is obtained from the gradient of the relationship between the phase difference (θ) and the substrate thickness (x). In addition, the phase difference (θ) at the coating thickness (d) is measured by changing the frequency (f). Therefore, the substrate thermal diffusivity (α_c) is obtained from the gradient of the relationship between the phase difference (θ) and frequency ($\sqrt{f}$) in Eq. (2). Hence, the thermal conductivity (k) can be described by using Eq. (3) [23]:

$$k = \alpha \times \rho \times C \quad (3)$$

where α is the thermal diffusivity, ρ is the density of the material, and c is the specific heat capacity of the coating or substrate. Based on the abovementioned, the thermal conductivity (k) is calculated with Eq. (1) from the thermal diffusivity (α), density (ρ), and specific heat capacity (C) in a real test.

3. Results and discussion

3.1. Microstructures of coatings

The thermal insulation capacity depends not only on the factors themselves but also on the microstructure, especially the porosity, interfacial gap and semimolten particles.

Fig. 3 shows the cross-sectional morphologies of the three coating types with different porosities (Fig. 3(a)–(b)). The coating sample (a) was uniform and dense, with the exception of a few pores within the top layer (Fig. 3(A)). The coating sample (b) exhibited a typical porous structure with special mesh splats. The splats had a special microstructure that differed from that of unmelted splats, which we call a honeycomb microstructure. Both coatings exhibited many pores and mesh splat inclusions, which were obviously more prevalent in the coating sample (c) sprayed with coolant (liquid nitrogen) (Fig. 3(B) and (C)). Table 2 shows the thicknesses and cross-sectional porosities of the Er_2O_3 coatings (100 and 300 μm). The porosities were determined by analyzing SEM images of the coatings. First, the thicknesses of the three coatings reached the expected target of approximately 100 μm (106, 108, and 108 μm). Moreover, the Er_2O_3 coating obtained by using O_2 as the carrier gas had a cross-sectional porosity of 7.7%. In the case of using N_2 as the carrier gas, sample (b) and sample (c) were sprayed under the same conditions, except only one was sprayed using the coolant; the resulting porosities were 15.6% and 28.3%, respectively. In a previous study, it was reported that changes in the temperatures and velocities of carriers for in-flight particles were useful for determining the impact behavior, and they also affected the morphology and porosity of the sprayed coating. Furthermore, to compare the microstructural and thermal insulation properties, the number of sprays was increased to obtain a coating thickness of 300 μm (calculated thicknesses were 334 μm sample (d) and 312 μm for sample (e)). Fig. 4 shows that the microstructures of samples made with and without coolant were significantly different (Fig. 4(d) and (e)). From Table 2, the porosities were close to each other because they were sprayed with the same spray parameters; thus, these spray conditions significantly controlled pore formation in the coatings, and thickness had no effect on the pores. In addition, an interesting phenomenon was observed: some of the inside splats formed mesh microstructures in all samples. However, in the case of splats sprayed with liquid nitrogen, the splats with mesh microstructures caused the number of formations to increase, and the sizes of the internal voids increased. Therefore, it is reasonable to assume that using the coolant to lower the substrate temperature controlled the number of pores in the coating and increased the sizes of the voids inside the splats.

Moreover, the layer connected to the substrate was denser than the top layer in all of the coatings. In this study, a chelate complex was

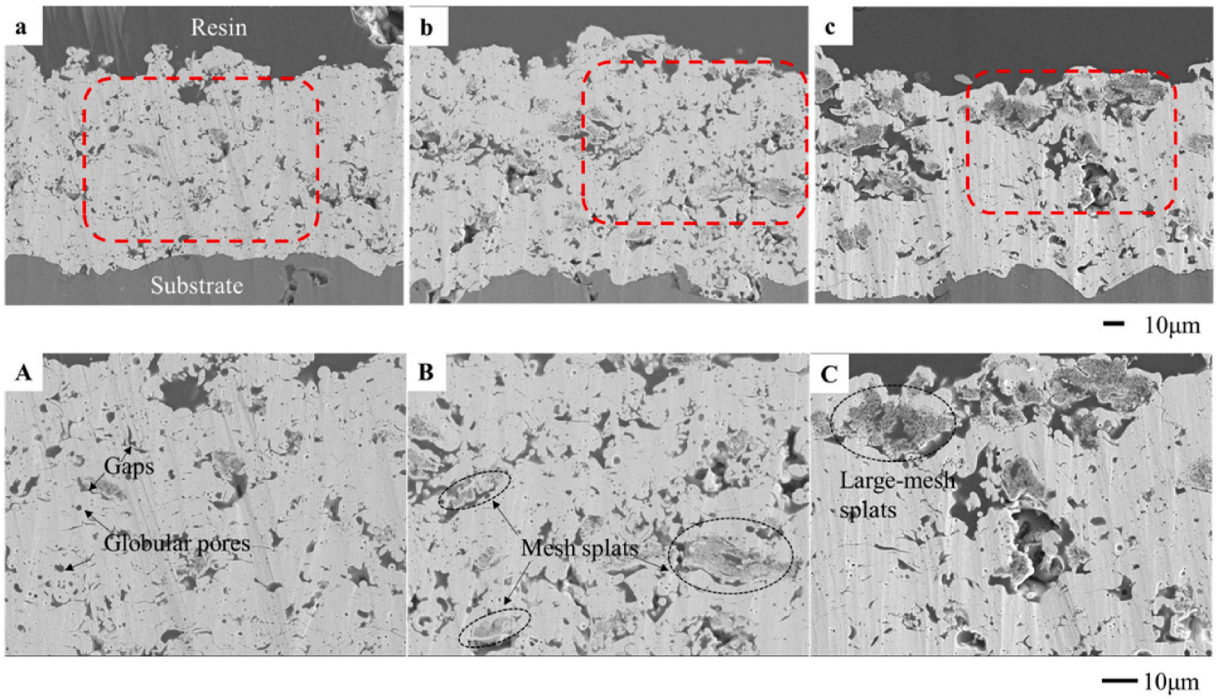

Fig. 3. SEM cross-sectional images of an Er_2O_3 coating with a thickness of approximately 100 μm: (a)/(A) and (b)/(B) sprayed with no coolant and (c)/(C) sprayed with liquid nitrogen. (The red dotted line areas are the higher magnification images). (For interpretation of the references to colour in this figure legend, the reader is referred to the Web version of this article.)

Table 2
Results of the thicknesses and cross-sectional porosities of Er_2O_3 coatings synthesized on an aluminum alloy (A5052) substrate. The sample in the blue area was deposited with liquid nitrogen.

Sample	Coating materials	Thickness (μm)	Cross-sectional Porosity (%)
(a)	Er_2O_3	106	7.7
(b)		108	15.6
(c)		108	28.3
(d)		334	16.9
(e)		312	25.5

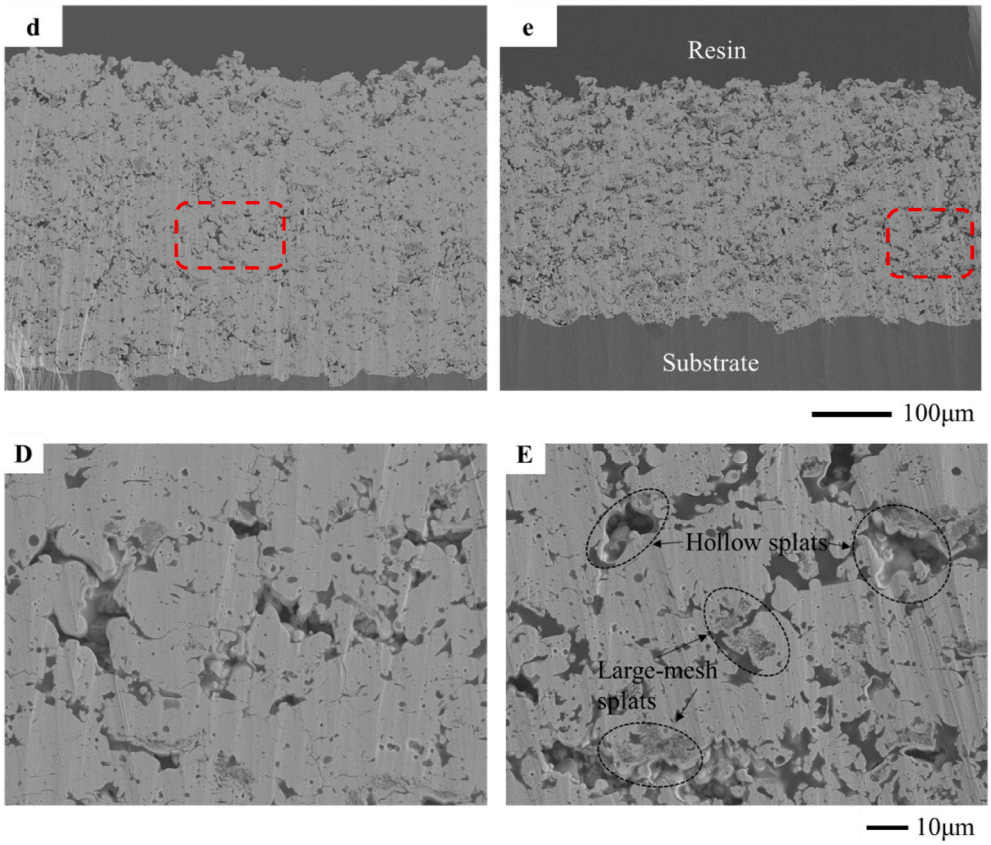

Fig. 4. SEM cross-sectional images of an Er_2O_3 coating with a thickness of approximately 300 μm: (d)/(D) sprayed with no coolant and (e)/(E) sprayed with liquid nitrogen. (The red dotted line areas are the higher magnification images). (For interpretation of the references to colour in this figure legend, the reader is referred to the Web version of this article.)

sprayed using a thermal spray technique; the jet was a flame formed by combustion of H_2 with O_2, and the injected feedstock was EDTA·Er·H powder. The EDTA·Er·H particles decomposed during flight, were oxidized and melted in the flame, spread into disk-shaped or splash-shaped impacts on the substrate surface, transferred heat to the underlying substrate and solidified rapidly. The coating was thus built up by agglomeration of solidified Er_2O_3 splats. During this process, the aluminum alloy substrate received heat from the solidifying splats, and it was also heated by the tail end of the flame since hot gas jets escaped from the impact area by flowing sideways over the substrate [24,25]. These two sources of heat significantly increased the temperature of the substrate and thus may have affected the porosities of splat layers located close to the temperature-sensitive aluminum alloy substrate [26]. This is expected to provide favorable thermal insulation performance.

3.2. Thermal conductivity

The fundamental function of a TBC is to provide insulation and prevent thermal flow into the substrate material. Therefore, thermal insulation capability is considered one of the most important factors for evaluating the performance of TBCs. In this investigation, the thermal insulation capabilities of TBCs were evaluated by temperature drops across TBCs ($\Delta T = T_1\text{-}T_2$). In addition, with the heating temperature curve, Eqs. (1)–(3) were used to calculate thermal conductivities with various thicknesses and porosities of coatings (samples (a)-(e)). To calculate the phase differences (θ) of samples in this study, all-temperature values in the figure below were chosen as the lowest inflection points of the curve peaks, and ten values around each reference temperature (RT) point, such as the rise phase (RT = 300 °C) and semisteady phase (RT = 400 °C) of the substrate, were selected, as shown in Fig. 5 (s), (s_1).

Figs. 6 and 7 illustrate the heating temperature curves (warming trend) recorded for the substrate sample surface (T_{1s}), the TBC sample surface (T_{1c}), the substrate sample back side (T_{2s}), and the TBC sample back side (T_{2c}) at temperatures ranging from 300 to 400 °C. Figs. 6 and 7 show that T_1 and T_2 increased with increasing spray flame time. The surface temperature of the TBC rose faster than that of the substrate. In addition, the surface temperature of the substrate tended to be stable at the reference temperature of 400 °C. Furthermore, Table 3 shows the temperature for the back side of each sample when the temperatures of the TBC and substrate were raised to 300 and 400°. In this case, the ΔT_c values of each sample were 182 °C, 195 °C, and 221 °C, as the substrate surface temperature tended to be stable at approximately 400 °C. This means that the TBCs contributed to a decrease in the temperature of the metal substrate. Moreover, the temperature drops across TBCs increased in coatings with different porosities as the spray flame time and temperature were increased. In addition, the surface temperature of the TBC with a given spray flame time tended to stabilize at approximately 500 °C, the temperature selection point, as shown in Fig. 8. These results showed that the side temperature curves for all TBCs became stable, and as the porosity increased, the difference between the curves for both sides increased significantly, especially with a porosity of 28.3% (Fig. 8 (c_2)). In addition, Figs. 6 and 8 show an interesting phenomenon in which the TBC temperatures were higher than the temperature of the substrate because the pores and voids formed in the coatings, especially those of the top layers, spread. This can be explained by thermal radiation across the pores, voids and mesh splats, which became slower as the coating was heated; this resulted in a reduction in the surface heat transfer rate, thereby increasing the surface temperature. Furthermore, the thermal conductivities of Er_2O_3 coatings with various porosities were calculated with the previously described equation. The density (ρ) was measured according to the Archimedes principle. The phase difference (θ) was measured from temperature curves with the AC calorimetric method. The deviation in thermal conductivity was estimated to be ± 0.6% due to deviations in ρ, α, and C, and the results are listed in Table 4. From these results, the thermal conductivities at 500 °C varied between 1.56 $Wm^{-1}K^{-1}$ and 0.90 $Wm^{-1}K^{-1}$, depending on the porosity.

Heating temperature curves for the increasing phase (sample (d) and sample (e)) and the stable phase (sample (d_1) and sample (e_1)) are shown in Fig. 9, and the thickness of the coating was increased to 300 μm (real thickness, as shown in Table 2). In the rising phase, T_1 and T_2 increased with increasing spray flame time. In addition, the rising ratio of T_2 was much lower than that of T_1, and a flat curve resulted with

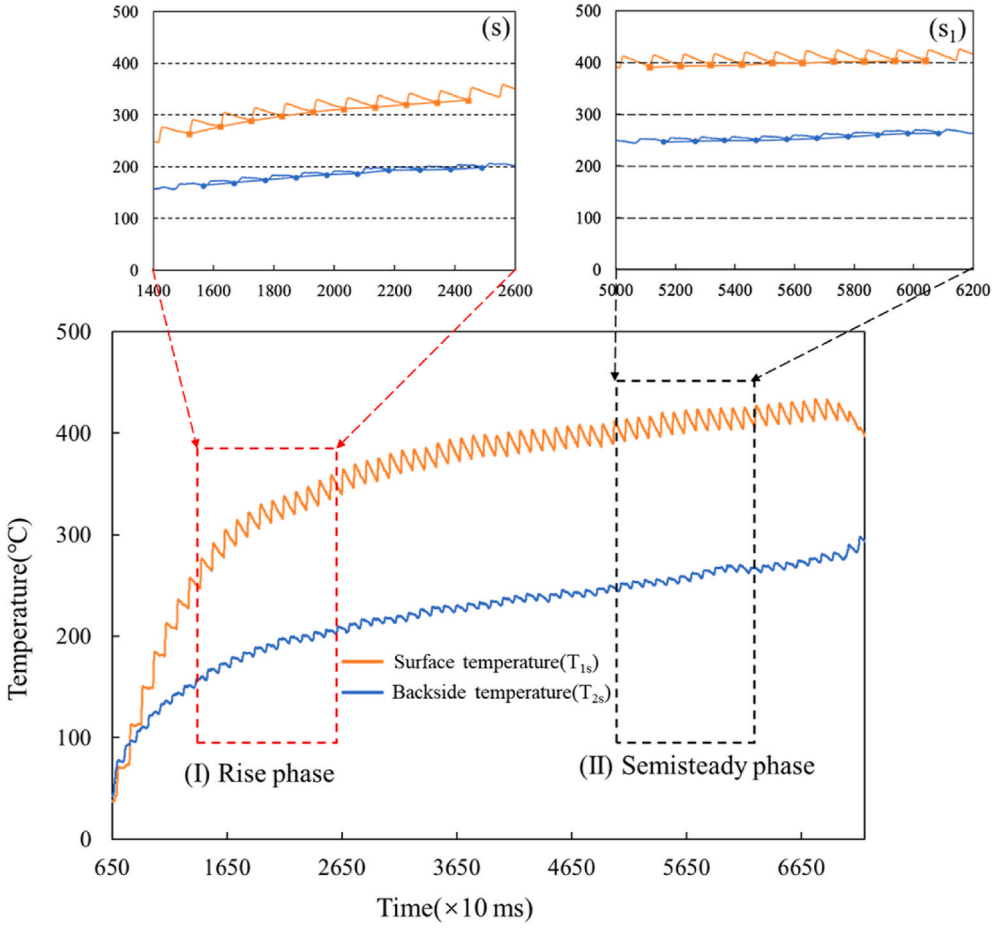

Fig. 5. Heating temperature curves of substrates (T_{1s}, T_{2s}): (s) reference temperature of 300 °C (rise phase) and (s_1) reference temperature of 400 °C (semisteady phase.

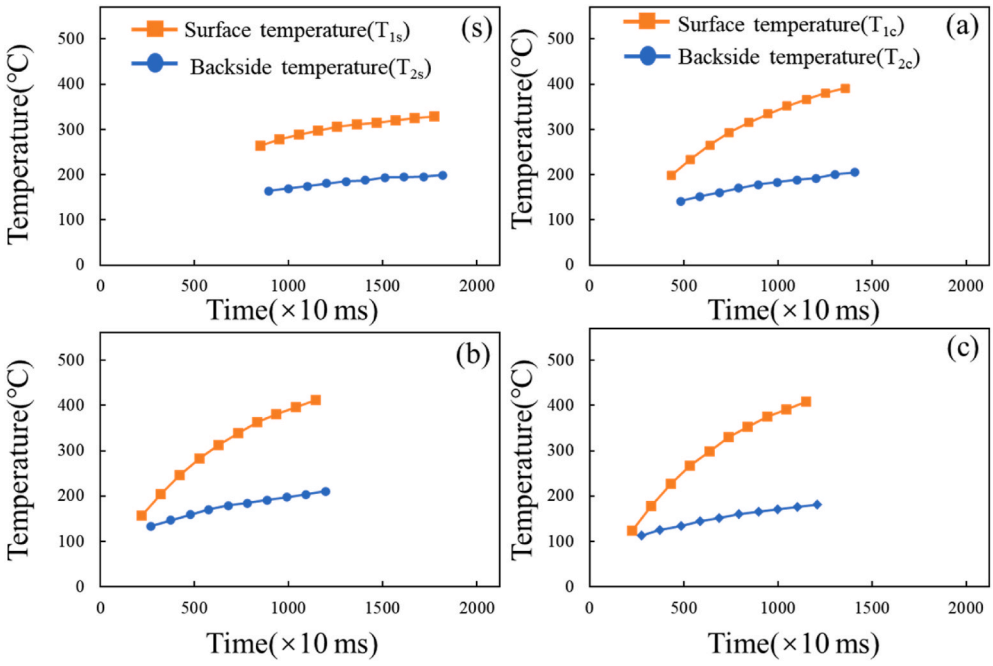

Fig. 6. Heating temperature curves for the substrate and the Er_2O_3 coating with a thickness of 100 μm: (s) substrate, (a) porosity of 7%, (b) porosity of 16%, and (c) porosity of 28% at a reference temperature of 300 °C.

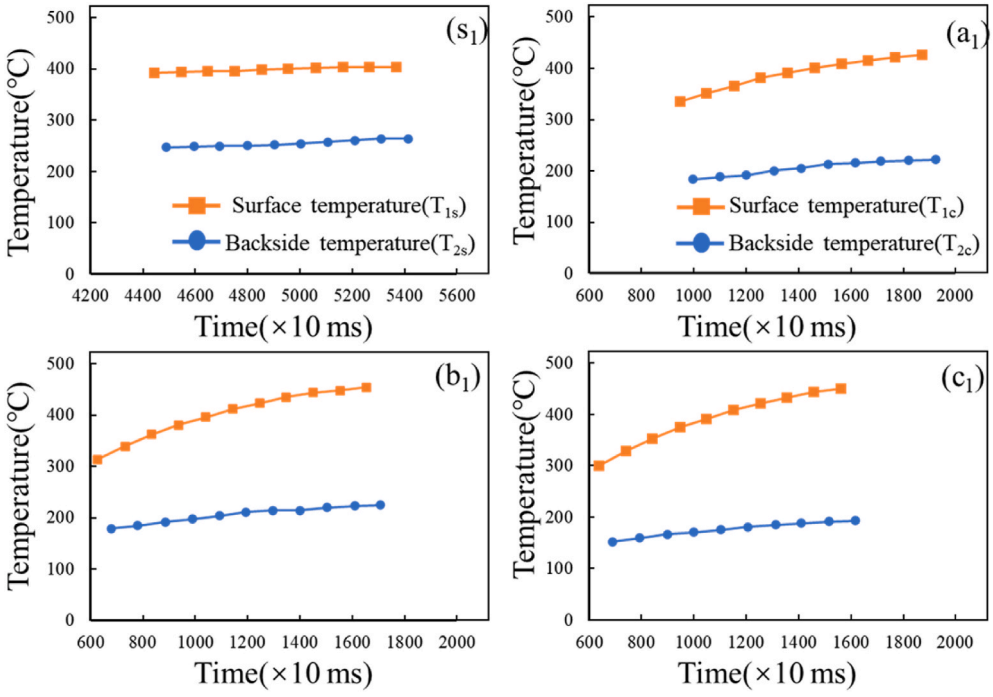

Fig. 7. Heating temperature curves for the Er_2O_3 coating with a thickness of 100 μm at a reference temperature of 400 °C: (s_1) substrate, (a_1) porosity of 7%, (b_1) porosity of 16%, and (c_1) porosity of 28%.).

increasing back-side temperature. This indicates that the thermal insulation capability depended on the microstructure and was especially related to porosity and splat gaps or voids formed; thus, Fig. 4 describes the microstructure as described, and the orientations of newly formed hollow splats (splats are hollow, and the splat wall is significant) were sloped in the direction of heat flux, which enhanced the thermal insulation capability and decreased the thermal conductivity. On the other hand, this is responsible for the easy flow of heat onto the surface through the pores of the coating, and the top layer is a thermal storage layer that proved to be more effective for heat blocking. Table 5 shows the rising phase for a sample with back-side temperatures at reference temperatures of 400 °C and 500 °C (only sample (e)). Sample (d) has a ΔT_d of 244 °C at the reference temperature of 400 °C, and sample (e) has ΔT_e values of 260 °C and 347 °C at the reference temperatures of 400 °C and 500 °C, respectively. Furthermore, in the stable phase, the temperature curves for both sides tended to be flat at 500 °C and 600 °C, as shown in Fig. 9(d_1) and (e_1). Moreover, the thermal conductivities were calculated to be 4.56 $Wm^{-1}K^{-1}$ and 2.57 $Wm^{-1}K^{-1}$, and details are

Table 3
Temperatures of the surface (T_1) and backside (T_2) at reference temperatures of 300 and 400 °C in the rise phase.

Sample	Reference temperature of 300 °C			Reference temperature of 400 °C		
	Time (× 10 ms)	Surface temperature (T_1/ °C)	Backside temperature (T_2/ °C)	Time (× 10 ms)	Surface temperature (T_1/ °C)	Backside temperature (T_2/ °C)
Substrate	1159	300.9	182.5	4957	400.0	258.1
(a)	746	300.3	170.7	1459	400.4	217.5
(b)	532	301.0	172.3	1043	401.7	206.6
(c)	639	300.8	154.2	1052	400.0	178.2

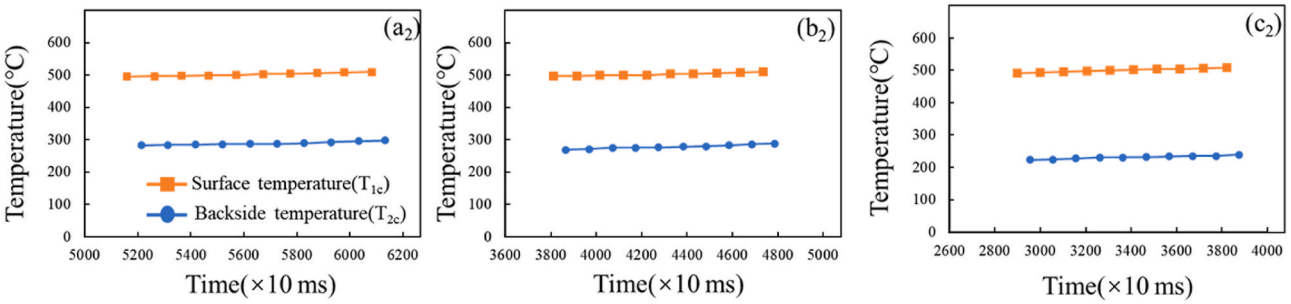

Fig. 8. Heating temperature curves for an Er_2O_3 coating with a thickness of 100 μm at a reference temperature of 500 °C: (a_2) porosity of 7%, (b_2) porosity of 16% and (c_2) porosity of 28%.

Table 4
Results for each sample in the stable phase (500 °C).

Sample	Time (× 10 ms)	Surface temperature (T_1/°C)	Backside temperature (T_2/°C)	ΔT (°C)	Thermal conductivity (W/(mK))
(a)	5571	500.5	291.5	209	1.56
(b)	4225	500.1	281.7	218	1.25
(c)	3308	500.1	235.5	264	0.90

shown in Table 6. In addition, Fig. 10 shows the different reference temperature drops for samples (d) and (e). Sample (d) has a higher surface temperature curve than sample (e); however, they have similar backside temperature curves at approximately 150 °C. The differences in thermal conductivity values depended on the spraying conditions, which controlled the porosities of the coatings.

The thermal insulation capability was determined as a function of porosity and thickness for mesh splats and hollow splats in each coating. Two groups of coatings with thicknesses of 100 μm and 300 μm were found to show different behaviors (in Figs. 8 and 9(d_1), (e_1)). First, the ΔT value depended on the coating thickness and porosity or

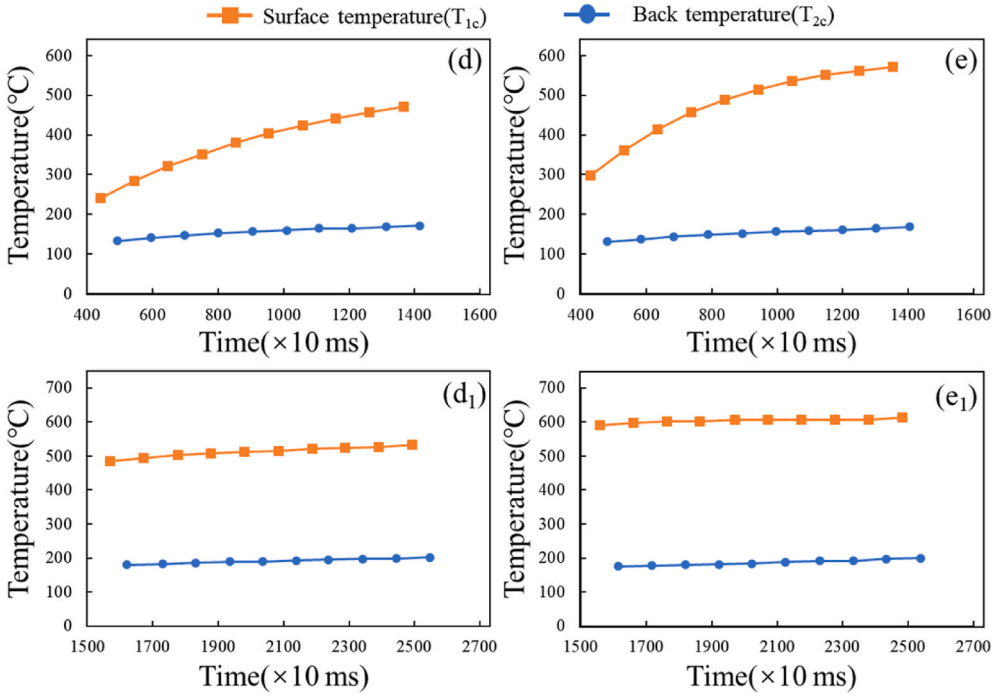

Fig. 9. Heating temperature curves for Er_2O_3 with a coating thickness of 300 μm: (d) porosity of 17% and (e) porosity of 26% at reference temperatures of 400–500 °Cand (d_1) porosity of 17% and (e_1) porosity of 26% at reference temperatures of 500–600 °C.

Table 5
Temperatures of the surface (T_1) and backside (T_2) at reference temperatures of 400 and 500 °C in the rise phase.

Sample	Reference temperature of 400 °C			Reference temperature of 500 °C		
	Time (× 10 ms)	Surface temperature (T_1/°C)	Backside temperature (T_2/°C)	Time (× 10 ms)	Surface temperature (T_1/°C)	Backside temperature (T_2/°C)
(d)	858	404.1	159.6	–	–	–
(e)	539	400.3	139.5	845	502.0	154.6

Table 6
Results for each sample in the stable phase (500 °C, 600 °C).

Sample	Time (× 10 ms)	Surface temperature (T_1/°C)	Backside temperature (T_2/°C)	ΔT (°C)	Thermal conductivity (W/(mK))
(d)	1676	500.0	187.7	312	4.56
(e)	1764	601.1	182.4	418	2.57

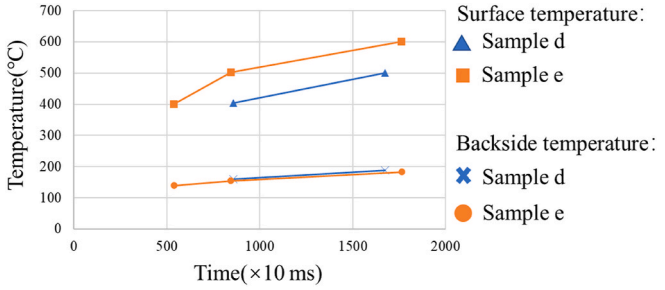

Fig. 10. Reference temperature curves at 400 °C, 500 °C and 600 °C.

microstructure. ΔT values increased with increasing coating thickness from 100 μm to 300 μm. The use of N_2 as the carrier gas and coolant for spray coating resulted in higher ΔT values than conventional coatings (e.g., O_2 as the carrier gas). For 300 μm coatings, the ΔT value in the stable phase for the Er_2O_3 coating was 43.1% of that for the 100 μm coating prepared with the same spray conditions (samples (b) and (d)). This means that thickness affected the thermal insulation measured in this study. Tables 4 and 6 show that the thermal conductivity values for 300 μm coatings were larger than those for 100 μm coatings in all samples. Generally, the factors affecting coating thermal conductivity were the spray conditions, such as the type of coating and spraying, the raw material size and the heat flow direction, and the coating microstructure, such as pore characteristics and the moisture ratio. Based on the abovementioned, two groups comprising samples (b) and (c) and samples (d) and (e) were sprayed under the same conditions; hence, the coating microstructures affected the thermal conductivity values. Two effects that would explain this phenomenon could have occurred during the thermal insulation test. First, the spray flame with H_2–O_2 resulted in moisture generated during spraying; when there is moisture (including water vapor) in the pores of the coating, the diffusion of steam into pores or gaps and the movement of water molecules play major roles in heat transfer, which is responsible for a significant increase in effective thermal conductivity. The other effect to consider arises with thick coatings with more pores or gaps; the deposition process involving the chemical reaction of EDTA·Er·H can be represented by Eq. (4) as follows:

$$2\ \mathrm{EDTA{\cdot}Er{\cdot}H} + 24\ \mathrm{O_2} \rightarrow \mathrm{Er_2O_3} + 20\ \mathrm{CO_2}\uparrow + 13\mathrm{H_2O}\uparrow + 4\ \mathrm{NO_2}\uparrow \quad (4)$$

Hence, the water vapor generated during deposition of layers or splats might enter the pores formed in or between layers, which would further increase the thermal conductivity. In other words, a new thermal insulation capability and thermal conductivity test was identified in this study. TBCs with thicknesses of 108–334 μm were successfully synthesized by depositing them on an aluminum alloy substrate, and good thermal insulation capacity was obtained without bond coating. This could greatly reduce the weights of the hot components used.

4. Conclusions

Er_2O_3 coatings with different thicknesses were synthesized by using a metal-EDTA complex with a flame-spraying system. By varying the spray conditions, the cross-sectional porosity of the deposited TBC could be varied from 7.7% to 28.3% and 16.9%–25.5% for thicknesses of 100 μm and 300 μm, respectively. In addition, Er_2O_3 exhibited good thermal insulation properties. The 300 μm coating exhibited a ΔT value that was 43.1% of that of the 100 μm coating made with the same spray conditions. In addition, the 100 μm coating exhibited low thermal conductivities, which ranged from 4.56 $Wm^{-1}K^{-1}$ with a porosity of 16.9% to 2.57 $Wm^{-1}K^{-1}$ with a porosity of 25.5% in the stable phase (500 °C and 600 °C). This study also provides a new method for testing thermal conductivity and thermal insulation capability. Therefore, expanded and deepened further studies of TBCs deposited on lightweight metals are expected.

Declaration of competing interest

The authors declare that they have no known competing financial interests or personal relationships that could have appeared to influence the work reported in this paper.

Acknowledgments

The authors gratefully acknowledge the raw material support by CHUBU CHELEST Co., Ltd. of Japan. This work was supported by Ningbo 3315 Talents Program (grant # 2020A-29-G), Chinese Academy of Sciences President's International Fellowship Initiative (grant #2020VEA0005), and K.C. Wong Education Foundation (grant # GJTD-2019-13).

References

[1] R. Vaßen, M. Ophelia-Jarligo, T. Steinke, D. Emil-Mack, D. Stöver, Overview on advanced thermal barrier coatings, Surf. Coating. Technol. 205 (2010) 938–942.
[2] S. Sampath, U. Schulz, M.O. Jarligo, S. Kuroda, Processing science of advanced thermal-barrier systems, MRS Bull. 37 (2012) 903–910.
[3] N.P. Padture, M. Gell, E.H. Jordan, Thermal barrier coatings for gas-turbine engine applications, Science 296 (2012) 280–284.
[4] X.Q. Cao, D. Stöver, R. Vaßen, F. Tietz, W. Jungen, E.V. Fischer, Lanthanum cerium oxide as thermal barrier coating material for high temperature applications, Adv. Mater. 15 (2003) 1438–1442.
[5] A.G. Evans, D.R. Clarke, C.G. Levi, The influence of oxides on the performance of advanced gas turbines, J. Eur. Ceram. Soc. 28 (2008) 1405–1419.
[6] K. Kokini, J. Dejonge, S. Rangaraj, B. Beardsley, Thermal shock of functionally graded thermal barrier coatings with similar thermal resistance, Surf. Coating. Technol. 154 (2002) 223–231.
[7] N.P. Padture, M. Gell, E.H. Jordan, Thermal barrier coatings for gas-turbine engine applications, Science 296 (2002) 280–284.
[8] B. Li, X.L. Fan, K. Zhou, T.J. Wang, Effect of oxide growth on the stress development in double-ceramic-layer thermal barrier coatings, Ceram. Int. 43 (2017) 14763–14774.
[9] R. Vaßen, M.O. Jarligo, T. Steinke, D.E. Mack, Overview on advanced thermal barrier coatings, Surf. Coating. Technol. 205 (2010) 938–942.
[10] D.R. Clarke, M. Oechsner, N.P. Padture, Thermal-barrier coatings for more efficient gas-turbine engines, MRS Bull. 37 (2012) 891–898.
[11] J. Wang, J. Sun, Q. Jing, B. Liu, H. Zhang, Y. Yongsheng, J. Yuan, S. Dong, X. Zhou, X. Cao, Phase stability and thermo-physical properties of ZrO_2-CeO_2-TiO_2 ceramics for thermal barrier coatings, J. Eur. Ceram. Soc. 38 (2018) 2841–2850.

[12] B. Lv, R. Mücke, X. Fan, T.J. Wang, O. Guillon, R. Vaßen, Sintering resistance of advanced plasma-sprayed thermal barrier coatings with strain-tolerant microstructures, J. Eur. Ceram. Soc. 38 (2018) 5092–5100.
[13] A. Cipitria, I.O. Golosnoy, T.W. Clyne, A sintering model for plasma-sprayed zirconia TBCs. Part I: free-standing coatings, Acta Mater. 57 (2009) 980–992.
[14] M.P. Planche, H. Liao, B. Normand, C. Codde, Relationships between NiCrBSi particle characteristics and corresponding coating properties using different thermal spraying processes, Surf. Coating. Technol. 200 (2005) 2465–2473.
[15] Y.X. Dan, K. Komatsu, K. Keita, T. Costa, Y. Ikeda, A. Nakamura, S. Ohshio, H. Saitoh, Heat-shock properties in yttrium-oxide films synthesized from metal-ethylenediamine tetraacetic acid complex through flame-spray apparatus, Appl. Phys. A 123 (7) (2017) 194.
[16] K. Komatsu, T. Sekiya, A. Toyama, Y. Hasebe, A. Nakamura, M. Noguchi, Y. Li, S. Ohshio, H. Akasaka, H. Muramatsu, H. Saitoh, Deposition of metal oxide films from metal-EDTA complexes by flame spray technique, J. Therm. Spray Technol. 23 (8) (2014) 833.
[17] Y.X. Dan, X.L. Zhou, A. Nakamura, K. Komatsu, H. Saitoh, Splat morphology and microstructure of chelate flame sprayed Er_2O_3 films, J. Ceram. Soc. Jpn. 128 (2020) 945–953.
[18] Y.X. Dan, T. Costa, Z.Y. Guo, A. Nakamura1, K. Komatsu, H. Saitoh, Thermal barrier coatings formed by flame spray with metal-EDTA, Jpn. J. Appl. Phys. 59 (2020) 75507.
[19] K. Komatsu, T. Costa, Y. Ikeda, K. Abe, Y.X. Dan, T. Kimura, A. Nakamura, T. Shirai, H. Saitoh, Synthesis of Y_2O_3 films on an aluminum alloy substrate using flame-spray apparatus with a H_2-O_2 flame, Int. J. Appl. Ceram. Technol. (2018) 1–10, 00.
[20] Y.X. Dan, T. Costa, A. Nakamura, K. Komatsu, H. Saitoh, Effect of in-flight particle behavior on the morphology of flame sprayed Er_2O_3 splats, Ceram. Int. 47 (2021) 11862–11869.
[21] W.J. Parker, R.J. Jenkins, C.P. Butler, G.L. Abbott, Flash method of determining thermal diffusivity, heat capacity, and thermal conductivity, J. Appl. Phys. 32 (1961) 1679–1684.
[22] Kazuya Okamoto, Hiroaki Anno, Fabrication of Anisotropic Thermal Diffusivity Measurement System for Thin Films by an AC Calorimetric Method, Tokyo University of Science, 2018, pp. 61–65.
[23] Z.Y. Shen, L.M. He, Z.H. Xu, R.D. Mu, G.H. Huang, Rare earth oxides stabilized $La_2Zr_2O_7$ TBCs: EB-PVD, thermal conductivity and thermal cycling life, Surf. Coating. Technol. 357 (2019) 427–432.
[24] Y. Bao, T. Zhang, D.T. Gawne, Non-steady state heating of substrate and coating during thermal-spray deposition, Surf. Coating. Technol. 194 (2005) 82–90.
[25] T. Zhang, Y. Bao, D.T. Gawne, P. Mason, Effect of a moving flame on the temperature of polymer coatings and substrates, Prog. Org. Coating 70 (2011) 45–51.
[26] S.K. Panigrahi, R. Jayaganthan, A DSC study on the precipitation kinetics of cryorolled Al 6063 alloy, Effect of rolling temperature on microstructure and mechanical properties of 6063 Al alloy, Mater. Sci. Eng. 45 (2008) 300–305.